Polymers & biopolymers

Nanoporous structure development in PEI thin film foams

Zainab S. Patel[1],[*], Santhosh Sridhar[2], Krishna Nadella[2], Vipin Kumar[2], Alexander Nuhnen[3], and Christoph Janiak[3]

[1] *Department of Materials Science and Engineering, University of Washington, Seattle, WA 98195, USA*

[2] *Department of Mechanical Engineering, University of Washington, Seattle, WA 98195, USA*

[3] *Institute of Inorganic and Structural Chemistry, Heinrich Heine University Düsseldorf, 40204 Düsseldorf, Germany*
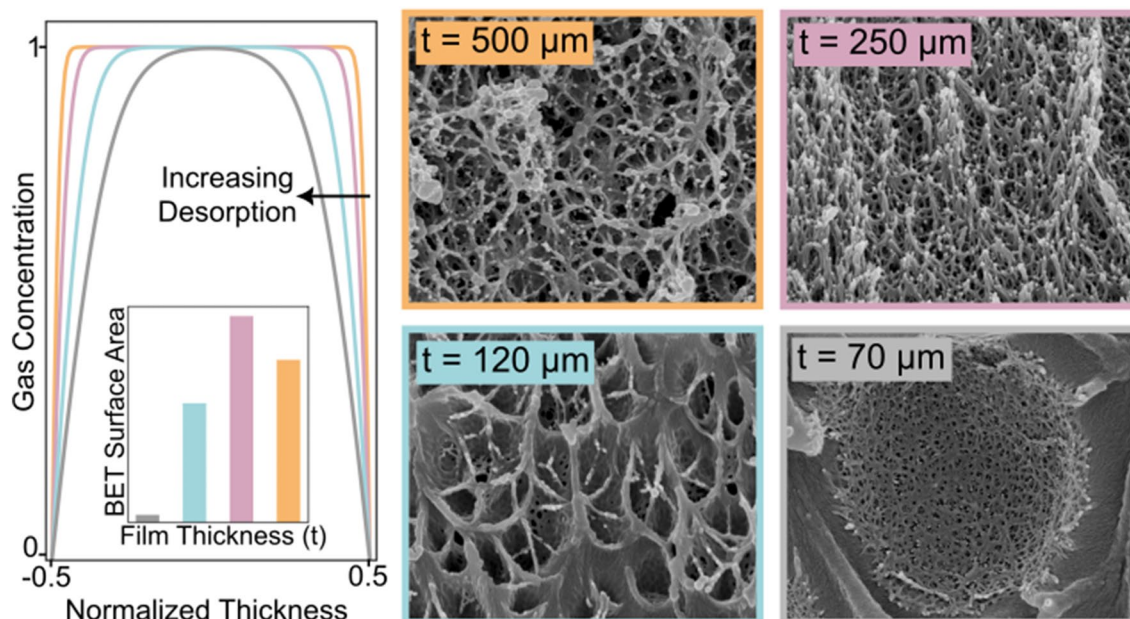
ABSTRACT

Solid-state foaming has been extensively explored as an eco-friendly, highly tunable route to produce microcellular and nanocellular structures in a broad range of thermoplastic polymers, yet most of this work is done at the macro-scale, where the evolution of cellular morphology remains unaltered by material dimensions. In this study, via a combination of experiments and numerical modeling, we investigate nanostructure development in polyetherimide (PEI) thin films with thicknesses ranging between 25 and 500 μm. Solid-state foaming of saturated polymer films yielded distinct structures, exhibiting both open-cell and closed-cell hierarchical morphologies, with cell nucleation density remarkably spanning four orders of magnitude. All films demonstrated primary and secondary cell structures, except for the 25 μm film, where no structure developed. Foam surface area was characterized using surface porosimetry, and PEI thin films exhibited a broad range of porosities. Except for the 70 μm film, all films were porous, exhibiting surface areas as high as 57 m^2/g for ultra-fine cell sizes of the order of ~70 nm. Modeling pre-foaming gas concentration profiles across the film thickness revealed gas concentration to be the primary driver of nanostructure development, demonstrating the high degree of structural tunability offered by the solid-state process, which is imperative to create advanced materials with enhanced properties.

🖄 Springer

GRAPHICAL ABSTRACT

Introduction

Porous polymer thin films are an emerging class of materials for numerous applications ranging from energy storage to tissue engineering [1–3]. The idea to incorporate very small bubbles in thermoplastics, of order 10 μm, goes back to the early work by Martini, Waldman, and Suh at MIT [4], where the advent of microcellular polystyrene was described using nitrogen as the blowing agent. The motivating question was, can we introduce 100 bubbles across a 1 mm thick thermoplastic sheet? If so, we could perhaps reduce the density of the sheet while retaining enough strength for applications that use thin-walled solid polymers, such as in packaging. The MIT solid-state batch process, originally developed for polystyrene, has been used to create microcellular foams from a number of amorphous and semi-crystalline polymers, such as polyvinylchloride (PVC) [5], polycarbonate (PC) [6, 7], acrylonitrile-butadiene-styrene (ABS) [8, 9], polyethylene terephthalate (PET) [10], polyethylene terephthalate glycol (PETG) [11], crystallizable polyethylene terephthalate (CPET) [12, 13], and polylactic acid (PLA) [14], to name a few. The cell sizes achieved in these studies typically range from 1 to 50 μm, and the foam structure is closed-cell.

The trend in the past two decades or so has been to reduce the size of the cells as far as possible. It started with ultra-microcellular foams with sub-micrometer-sized cells [15, 16]. Subsequently, nanocellular foams with cells of order 100 nm were created by the solid-state process in polyimides (PI) [17, 18] and polyether sulfone (PES) [19]. Handa and Zhang achieved cells in the 200–400 nm range in PMMA [16]. Miller et al. studied the polyetherimide (PEI)-CO_2 system, in which both microcellular and nanocellular structures were produced over a range of foam densities [20, 21]. Recent work has advanced fabrication techniques to create cells of order 10 nm. One effective strategy involves saturating the polymer at lower temperatures to achieve higher gas concentrations, which, in turn, leads to several orders of magnitude higher cell nucleation density, resulting in cells of order 10 nm [22, 23].

The creation of such ultra-fine cells also makes these foams a suitable candidate for applications where high surface areas are desired [1], yet porosity in solid-state foams remains understudied. Moreover, to date, all solid-state fabrication work on microcellular and nanocellular foams has been conducted on bulk polymers, i.e., polymer sheets with thicknesses of 1 mm or higher. As the sample thickness is reduced to a scale where the ratio of cell size to sample thickness becomes comparable, it prompts the

question of whether we can introduce 100–1000 bubbles across a 100 µm film. In this paper, we explore this very question. As the thickness of a polymer film reduces below a certain range, the physical properties of the film, like stiffness [24, 25], thermal conductivity [26], etc., significantly differ from that of the bulk, primarily due to confinement effects and interfacial interactions. Thus, the overarching goal of this study is to unravel the drivers behind nanostructure development in thin films foamed using the solid-state process and analyze their resultant properties. To achieve this, we specifically examine the PEI-CO_2 gas system, leveraging PEI's unique properties at high temperatures and its wide usage in the electronics industry [27, 28]. These results advance our understanding of foaming mechanisms and porosity in thin films, demonstrating their potential for diverse applications.

Experimental

Materials and equipment

Thin ULTEM 1000 PEI films of thicknesses 500 µm, 250 µm, 120 µm, 70 µm, and 25 µm were obtained from SABIC and then cut into 1 cm radius disks. It has a density of 1.28 g/cm^3 and a glass transition temperature of 215 °C. Praxair CO_2 was used as the blowing agent. The saturation pressure and temperature were controlled using an Omega controller. The weights of all samples, before and after saturation and after one-minute desorption, were measured on a METTLER AE240 balance with an accuracy of ± 10 µg to measure gas uptake. Samples were foamed in a heated press, where two parallel platens were maintained at a predefined temperature. The relative densities of the foamed samples were measured using ASTM D792-water displacement method [29]. These samples were then characterized under an FEI Sirion XL30 electron microscope. N_2-sorption isotherms were measured on an Autosorb 6 automatic volumetric gas sorption analyzer (from Quantachrome, Odelzhausen, Germany) at 77 K within a pressure range of 0.01–1 bar. Before each experiment, the samples were activated for at least 3 h at 373 K under a vacuum $< 5 * 10^{-3}$ mbar. Isotherm evaluation was performed with the ASWin automated gas sorption data acquisition and reduction software from Quantachrome Instruments, version 2.03.

Experimental design

Creation of micro-nano cellular structures in thermoplastic polymers via solid-state foaming is a three-step process: sorption, desorption, and foaming (Fig. 1) [30]. The specimen is placed in a pressure vessel to saturate with a gas such as CO2. The time required to reach equilibrium saturation varies as a square of the specimen thickness. The polymer is then removed from the vessel, and desorption begins to deplete the gas from the surface layer of the polymer, such that bubbles do not nucleate in the surface layer, leading to an unfoamed skin layer. The thickness of the unfoamed skin layer can be controlled by adjusting the desorption time [7]. In the final step, the polymer specimen is heated at a foaming temperature for a specified time to nucleate and grow the bubbles. Often, a temperature-controlled hot bath is used for this purpose. However, we used a hot press to produce foamed film specimens that were relatively flat. All the primary process variables of the solid-state process i.e., saturation temperature, saturation pressure, saturation time, desorption time, foaming time, and foaming temperature, were kept constant. Values of the process parameters are listed in Table 1 below.

We conducted a saturation study to understand gas diffusion characteristics in the polymer and a foaming study to analyze the microstructures hence produced.
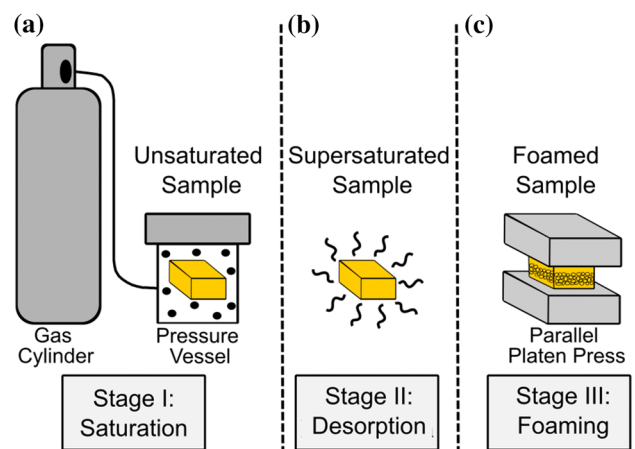

Figure 1 Experimental setup to perform solid-state foaming. **a** Saturation step where the polymer is filled with gas in a pressurized chamber. **b** Desorption step where the polymer is removed from the vessel and starts losing gas. **c** Foaming step where heating of the supersaturated sample creates a cellular structure in the polymer.

Table 1 Processing conditions to produce nanocellular thin films

Process variable	Value
Film thickness	500 μm, 250 μm, 120 μm, 70 μm, 25 μm
Saturation pressure	5 MPa
Saturation temperature	Room Temperature
Saturation time	40 h, 10 h, 3 h, 45 min, 6 min
Desorption time	1 min
Foaming temperature	180 °C
Foaming time	30 s

For the saturation study, all samples were saturated at room temperature and 5 MPa until they reached equilibrium. During the process, specimens were periodically removed from the pressure vessel and weighed to measure the gas uptake. However, handling thin film samples during the sorption process becomes challenging. Thick samples (thickness greater than 500 μm) used in previous studies can be returned to the pressure vessel and re-pressurized with minimum error. But thin film samples must be replaced every time as the error produced by repeated depressurization and re-pressurization cannot be neglected.

For the foaming study, fully saturated samples were removed from the vessel and taken to the foaming press. The desorption time for all films was kept constant at 1 min and was measured as the time elapsed from the instant the vessel was first depressurized to the time the sample was placed in the heated press. All samples were foamed at 180 °C for 30 s. Post-foaming, samples were left to desorb for 24 h to remove any residual gas. We then measured the relative density of these samples. Specimens were freeze-fractured under liquid nitrogen and then coated with a 20 nm Au/Pd layer to make the sample conductive. All micrographs were taken at the center of the samples to compare the structure in the core. Microstructure features were measured using Image-J and then analyzed comparatively between different thicknesses.

Model for gas concentration profiles

The formation of foam microstructures is heavily influenced by the concentration of gas molecules before foaming. To quantify this, we calculate the average gas concentration (AGC), which represents the average amount of gas absorbed by the polymer during the sorption process. AGC is determined by taking the difference between the initial and final weight of the polymer specimen, dividing it by the initial weight of the specimen, and is plotted in Fig. 2. For thick PEI specimens under the specified processing conditions, the AGC is 110 mg/g [20], which aligns with our observations in the 500 μm film investigated in this study. However, as we decrease the film thickness from 500 to 70 μm, the AGC after one-minute desorption decreases from 104 mg/g to 84 mg/g. Notably, the 25 μm film experiences a significant decrease in absorbed gas, reaching a final concentration of 57 mg/g.

AGC is a useful process parameter for achieving the desired foam morphology in bulk materials, but its effectiveness may not hold true for thin films due to the increased surface area-to-volume ratio as the films become thinner. To understand how the changing gas concentration profiles across the film thickness affect the final microstructure, a numerical model is developed [7]. Assuming one-dimensional diffusion because the polymer thickness is significantly smaller compared to the other dimensions, we use Fick's second law as follows:

$$\alpha \frac{\partial^2 C}{\partial x^2} = \frac{\partial C}{\partial t} \tag{1}$$

Numerical modeling is conducted using finite volume discretization on Python, and the diffusion coefficient (D)= 1.8 e^{-8} cm^2 s^{-1} is used following the values published by Miller et al. for thicker bulk specimens [20]. A Dirichlet–Dirichlet condition is employed for the end nodes, assuming an instantaneous drop in concentration to zero at the start of the desorption process. The result of modeling gas concentration profiles at different diffusion times is plotted in Fig. 2.

We first compared the total amount of gas absorbed in the polymer sample calculated by the model and obtained experimentally. As seen in Fig. 2, overall, an excellent agreement was obtained between the two values except for the 25 μm film, where we see some deviation. The difference in values for the 25 μm film might result from the accelerated diffusion, causing experimental and computational errors. We also computed the local gas concentrations at different time steps during the desorption process, as shown in Fig. 2.

In the case of the 500 μm and the 250 μm films, the gas concentration shows a drop only near the edges. As a result, the concentration remains uniform
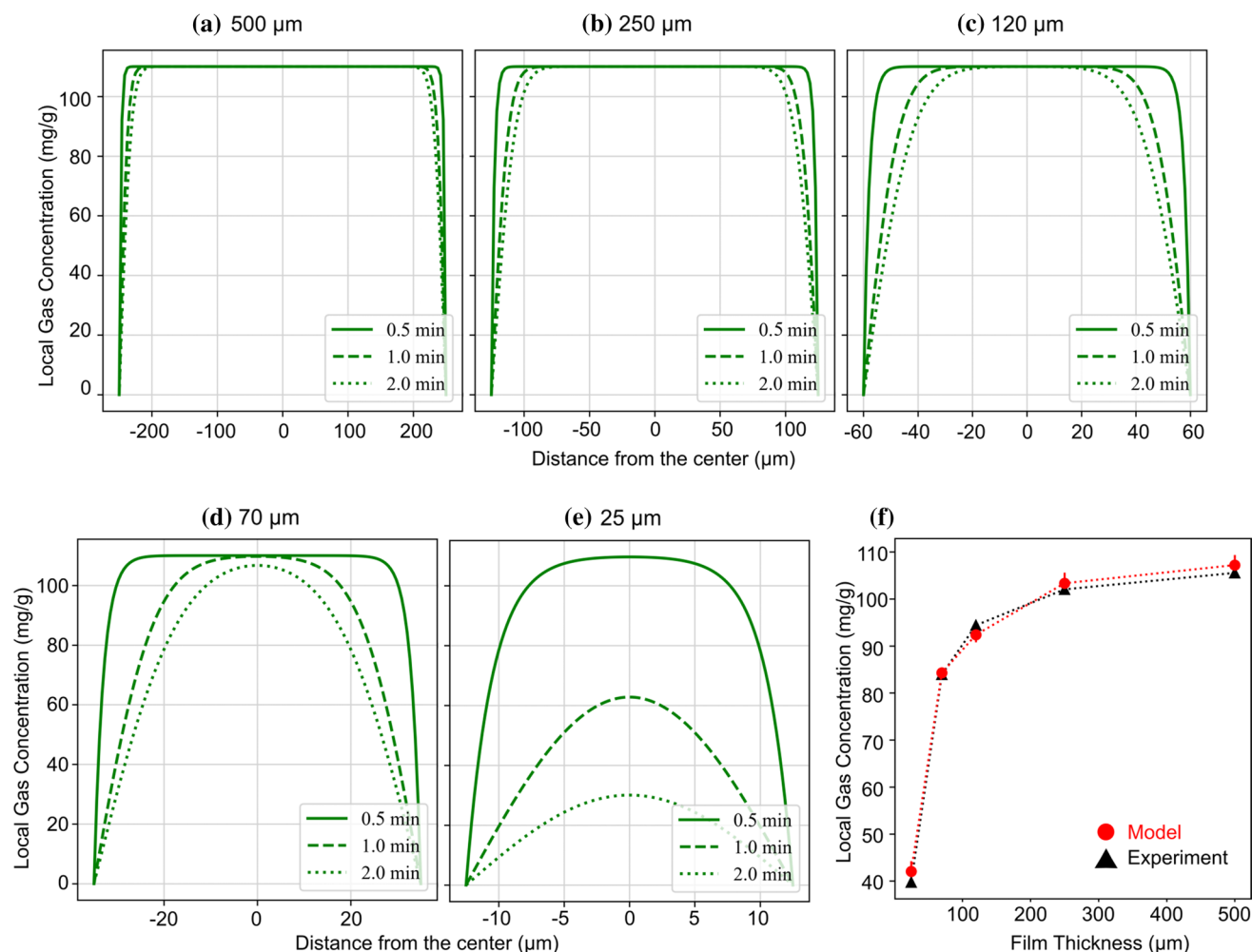
Figure 2 Gas Concentration profiles: **a–e** Profiles across the polymer thickness after 0.5, 1, and 2-min desorption in the 500 μm, 250 μm, 120 μm, 70 μm and 25 μm thick films, respectively. Note the excessive gas loss in the **d** 70 μm and **e** 25 μm samples. Legends in each profile show the different time steps for the gas concentration profiles; **f** Comparison of the average gas concentration values after 1 min desorption obtained from the model and measured experimentally.

and equal to the equilibrium value for most nodes across the film's thickness. However, as the thickness decreases to 120 μm and below, noticeable gas depletion becomes evident throughout the samples. Specifically, for the 70 μm film, only a small central portion of the specimen (10 μm thick) retains the equilibrium gas concentration, while the remaining portion (60 μm thick) exhibits a significantly lower gas concentration. In the case of the 25 μm film, an extreme scenario is observed, where even the gas concentration in the central region falls below the equilibrium value due to rapid desorption. These concentration profiles demonstrate substantial variations, which are expected to significantly impact the resulting cellular structures. The subsequent section

will further elaborate on the distinctive morphology of the foam structures formed within these thin films.

Morphology of nanocellular films

The open-cell nanocellular structure: 500 μm film

Given the high AGC in the 500 μm film specimens, like other bulk PEI specimens processed under similar conditions, an open-cell nanocellular structure is observed. This microstructure had an average cell size of 210 nm, and each primary cell contained smaller

nanopores around 20–50 nm, resulting in a broad distribution of cell sizes, as seen in higher magnification images in Fig. 3. As common for open-cell structures, the cell wall thickness is almost an order of magnitude smaller than the cell size, on an average of about 31 nm. The cell nucleation density of this structure was found to be 1.4×10^{14} cells/cm^3, calculated using a previously described method [30]. This structure is porous to multiple gasses and wetting liquids, as shown recently by Nicolae et al. [31].

The directional open-cell nanocellular structure: 250 µm film

Despite only a 7% drop in AGC, the 250 µm film develops a unique structure, deviating from expected PEI behavior under the given conditions. Although the structure is still open-celled and nanocellular, the nanopores are smaller and elongated in the thickness direction, as seen in Fig. 3. The average cell size of this structure is 72 nm, 3 times smaller than the 500 µm film, and the smallest among all the film thicknesses in this study. Moreover, this structure is uniform and

does not have a secondary cell structure. Previously Zhou et al. have also seen similar morphologies in thicker PEI films, although under different processing conditions, resulting in improved mechanical properties like flexural modulus and specific strength [32].

The transitional nanocellular structure: 120 µm film

In the 120 µm film, the structure transitions from a purely open-cell structure to a partially open-cell structure. We see closed cells 330 nm in size with 50 nm thick cell walls. However, every closed-cell contains multiple smaller pores 30 nm in size, as seen in Fig. 2. The cell nucleation density decreases by one order of magnitude, to 1.67×10^{13} cells/cm^3 as compared to the 500 µm sample.

The hierarchical micro-nano structure: 70 µm film

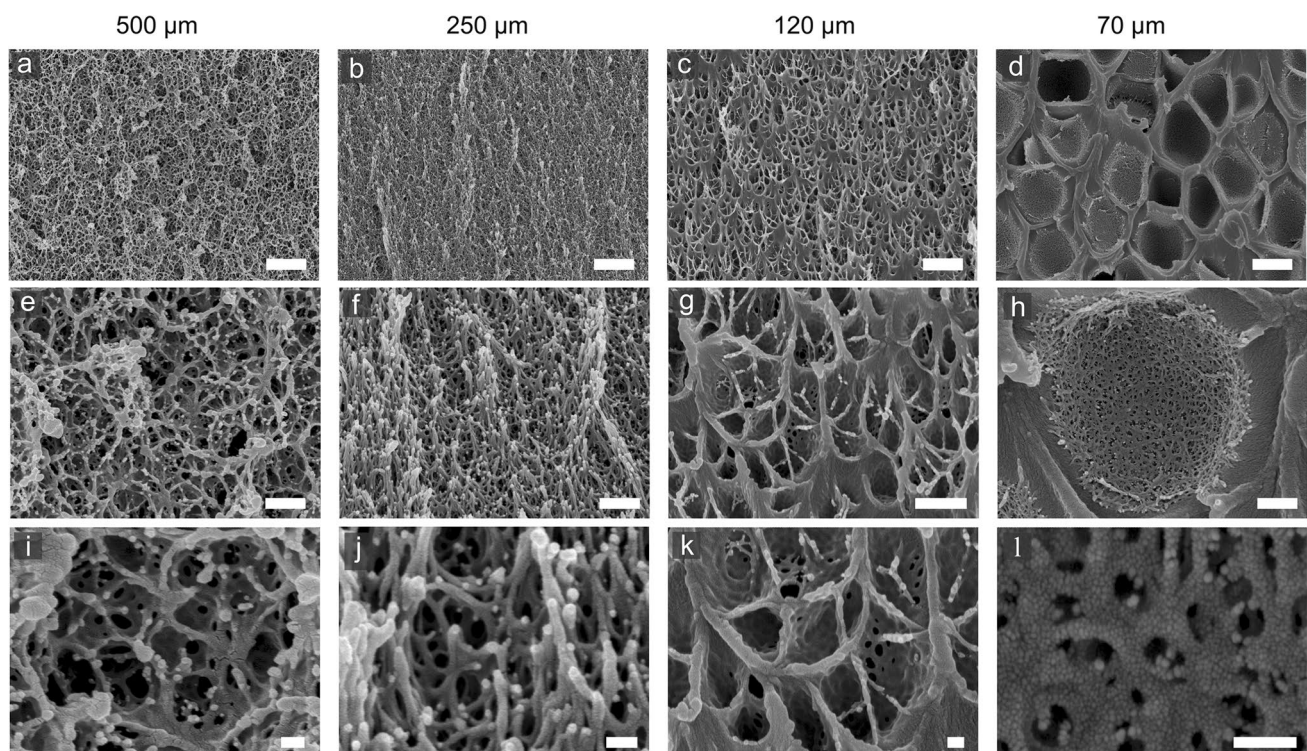An order of magnitude reduction in thickness and 20% drop in AGC produces a hierarchical

Figure 3 Nano-microcellular structure observed in PEI thin films: Cross sectional SEM Images of the microstructure in order of increasing magnification from top to bottom: 7000×, 30,000×, and 90,000×. **a**, **e**, **i** 500 µm film; **b**, **f**, **j** 250 µm film; **c**, **g**, **k**: 120 µm film; **d**, **h**, **l** 70 µm film. Scale bar: **a**, **d** 2 µm; **e**, **h** 500 nm; **i**, **l** 100 nm.

micro-nano cellular structure in the 70 μm film. The primary structure contains large micron-sized closed cells with thick cell walls. Each micropore contains smaller nano cells inside them, as seen in Fig. 3. The average cell size of the primary cells is 2 μm, while the pores within the cell walls are approximately 40–50 nm in size. The microcellular structure has a relatively thick cell wall and low cell nucleation density as compared to the other structures reported above. Although it appears to be closed-cell, the extensive network of nanopores inside each cell suggests a more 'open-cell' structure. A distinctive feature of this sample is the absence of any transitional structure between the core and the solid skin, as seen in Fig. 3. The microstructure is uniform across the thickness with the hierarchical structure as the core and 15 μm solid skin on both edges (Fig. 4). This hierarchical structure is generally observed in the transition region between the core and the skin for bulk specimens, implying that this is the structure developed at lower gas concentrations in PEI.

Microstructural features and relative density

Table 2 below summarizes the key microstructural features described above, and Fig. 5 illustrates the primary and secondary cells and cell wall thickness. All structures except the 250 μm film exhibit a broad distribution of cell sizes. The cell size of the primary structure increases down the thickness from 200 nm to 2 μm. Secondary cells inside the primary structure are consistently in the 30–50 nm range for the 500, 120, and 70 μm films. As the structure transitions from open-cell to closed-cell, the cell wall thickness increases from 31 nm to 218 nm respectively. Figure 6 shows the variation in relative density and cell nucleation density with AGC for the samples analyzed in this study. Notably, AGC decreases with decreasing thickness, producing foams characterized by lower nucleation density and larger cells. Overall, cell nucleation density varies over four orders of magnitude, the highest for the 250 μm film. It particularly drops for the 70 μm film to the order of 10^{11} cells/cm^3 as the primary
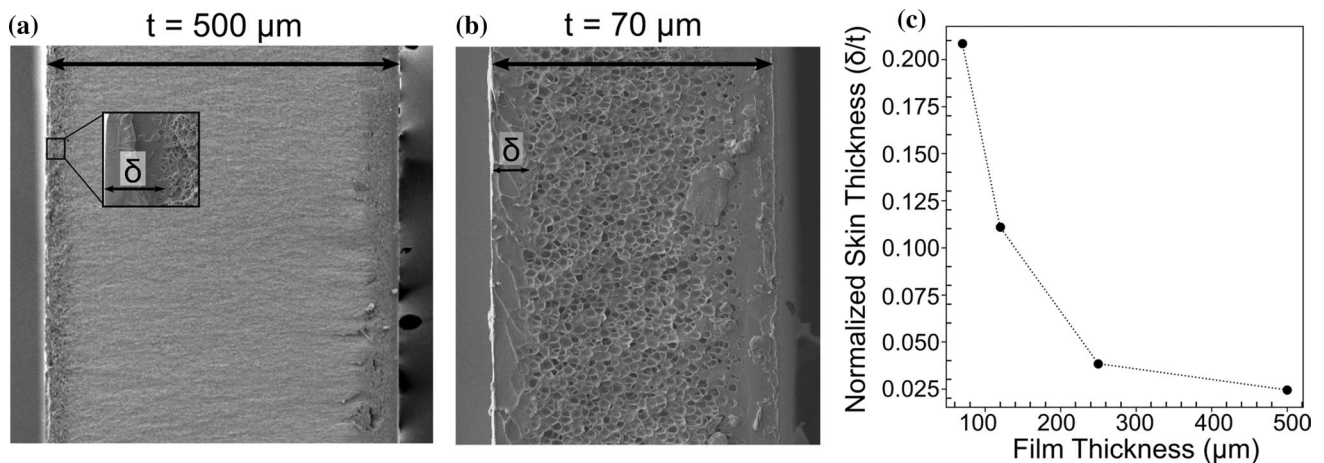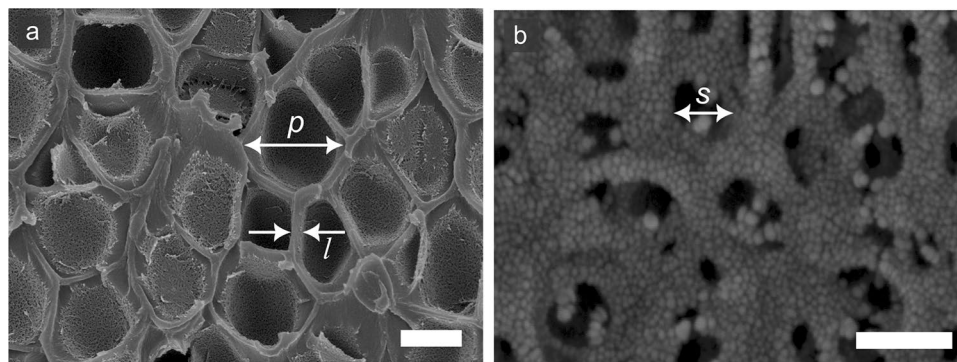

Figure 4 Skin thickness in PEI thin films: **a** Cross sectional SEM image of the 500 μm sample showing the total sample thickness (t) and solid skin thickness (δ). Inset shows a magnified view of the solid skin, Scale bar for inset 10 μm; **b** SEM Image of the 70 μm sample; **c** normalized skin thickness as a function of film thickness.

Table 2 Summary of the key microstructure feature measurements from the micrographs in Fig. 3

Film Thickness (μm)	Average gas concentration (mg/g)	Relative density	Primary cell size (nm)	Primary cell wall thickness (nm)	Cell nucleation density (cells/cm^3)	Skin thickness (μm)
500	104	0.47	235	31	1.4×10^{14}	12.2
250	100	0.50	73	NA	1.87×10^{15}	9.6
120	93.5	0.59	333	50	1.67×10^{13}	13.3
70	83.2	0.65	2020	218	1.63×10^{11}	14.6
25	57.5	1	–	–	–	–

Figure 5 Microstructure features: **a** Cross sectional SEM image of the 70 μm sample showing the primary cell size *(p)* and primary cell wall thickness *(l)* (Scale bar: 2 μm) **b** magnified SEM image of the 70 μm sample showing the secondary cell size *(s)* (Scale bar: 200 nm).

cellular structure transitions from the nanoscale to the microscale. Concurrently, relative density exhibits an upward trend as we progress through the thickness, as depicted in Fig. 6. The 500 μm film has a relative density of 0.47, which matches previously published literature values for bulk PEI specimens [20]. However, as the thickness decreases by an order of magnitude, the relative density increases to 0.65, as seen for the 70 μm film. With decreasing thickness, excessive desorption reduces the cell nucleation density during foaming, producing foams with a smaller void fraction. Since all the samples have been saturated to equilibrium at the same saturation pressure, this variation is not expected in the case of bulk samples with varying thicknesses. Thus, this trend between cell nucleation density, gas concentration, and relative density demonstrates how thin films behave differently than bulk specimens.

Another interesting feature of all solid-state foamed specimens is the unfoamed solid skin on both edges. It is developed as the local gas concentration for some sections of the polymer goes below the critical gas concentration required for foaming [7]. If we compare the normalized skin thickness (skin thickness (δ) divided by the sample thickness (t)), we observe an increase with decreasing film thickness. As the sample size becomes smaller, larger sections of the sample remain unfoamed (Fig. 4). This is because the size of the section below the critical gas concentration for foaming increases, showing a more pronounced effect of desorption in thin films.

Porosity of PEI foams

While SEM micrographs provide insightful information on the foam microstructure in 2D, they cannot be used to evaluate the total surface area of a material as well as its porosity. With the wide-ranging potential applications of porous polymer films, as exemplified in studies such as [2, 3], as well as the recent investigations into the transport properties of nanocellular PEI [31], the need to determine the pore surface area of such films is imperative. In light of this, we conducted physisorption experiments, where degassed, foamed samples underwent N_2 gas sorption at a low temperature (77 K) in small increments. Equilibrium pressure was measured at each increment, yielding an adsorption isotherm, which relates the volume of gas adsorbed to the relative pressure (p/p_0), where p represents the equilibrium pressure, and p_0 represents the saturation pressure. To determine the pore surface area, we analyzed these isotherms using the BET equation [33] in its linear form as follows:

$$\frac{p}{v(p_0 - p)} = \frac{1}{v_m c} + \frac{c - 1}{v_m c} * \frac{p}{p_0} \qquad (2)$$

In this context, v represents the total volume of gas adsorbed, v_m is the volume of gas adsorbed when a single monolayer of adsorbate has fully coated the adsorbent surface, and c is a constant. The isotherm can be divided into three regions based on relative pressure: low-pressure, intermediate, and high-pressure. In the low-pressure region, the isotherm is concave, while in the intermediate region, it is approximately linear. In the high-pressure region, it is convex with respect to the relative pressure axis. The start of the intermediate region indicates that the surface is entirely coated with a single monolayer of the adsorbate, and the volume of gas adsorbed at this point corresponds to v_m. Typically, a plot of $p/v(p_0 - p)$ versus p/p_0 within the relative pressure range of 0.05 to 0.35 yields a near-linear relationship, and the slope and intercept of this plot can be used to calculate v_m. Subsequently, the surface
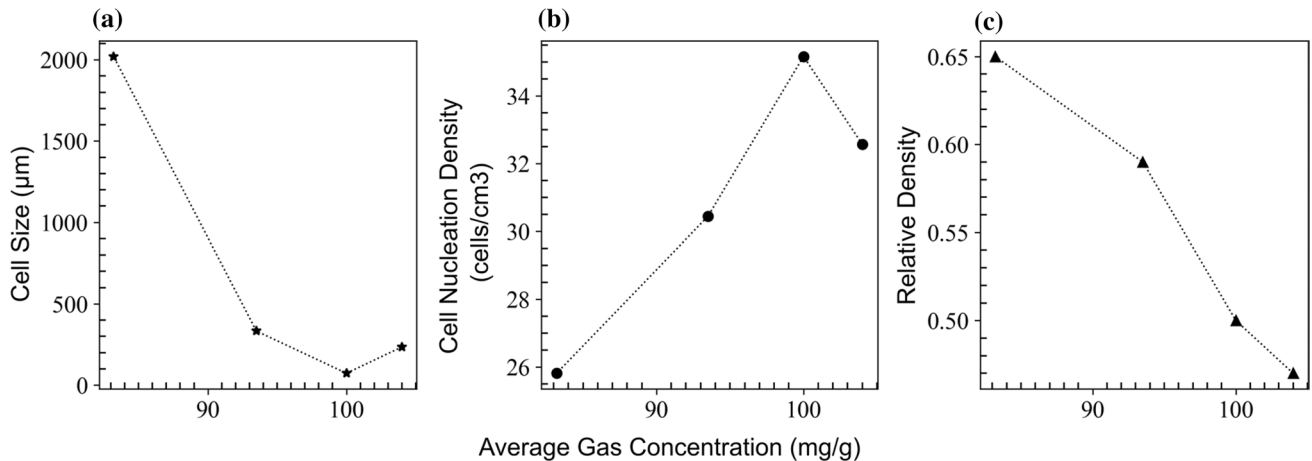
Figure 6 Microstructure features: Variation in **a** primary cell size, **b** cell nucleation density (log scale), and **c** relative density with average gas concentration in the sample.

area can be calculated using the methods described in [33, 34].

Figure 7 displays the BET isotherms for all films investigated in this study, revealing that all except the 70 μm film are porous. Cell size and cell nucleation density were identified as the primary factors influencing foam surface area, as evident in Fig. 7. Foams with smaller cell sizes and higher cell densities exhibited a greater surface area, whereas larger cell sizes and lower cell densities corresponded to reduced surface area. Notably, the 250 μm film exhibited the lowest primary cell size and the highest cell

nucleation density, resulting in a surface area of 57 m^2/g, the largest among all samples. Conversely, the 120 μm film with the lowest cell density and primary cell size had the lowest surface area. It is important to acknowledge that the nano-micro cellular foams examined not only have different cell sizes but also different morphologies, which significantly affect the total surface area. For instance, the 500 μm and 250 μm films have notably larger surface areas due to their open-cell morphologies, whereas the 70 μm film had no adsorption because of its large closed-cell pores. Generally, high surface area films exceed 300
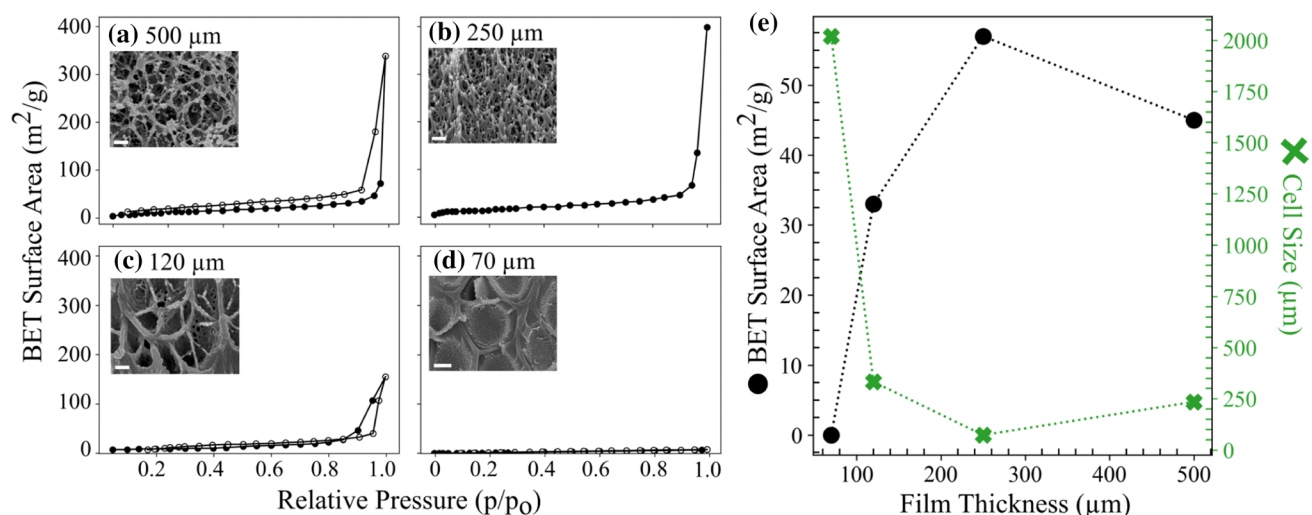

Figure 7 Adsorption isotherms and BET surface area **a–d** Nitrogen Sorption Isotherms with insets showing corresponding primary cell structure for the 500 μm, 250 μm, 120 μm, and 70 μm thick films, respectively. **e** BET surface area and cell size vs film thickness showing decreasing surface area with decreasing film thickness (Scale bar in all images: 2 μm).

m^2/g [35], so even the highest measured foam surface area of 57 m^2/g is relatively modest, albeit with the solid skin on the foamed specimens. Controlled engineering of nanostructures without a solid skin and high porosity could further accelerate the use of PEI films for sorption applications.

Discussion

The results presented above provide insights into utilizing the solid-state process for foaming thin films, showcasing its potential for creating lightweight materials with high control over cellular morphologies. In the 500 μm film (Fig. 2), the concentration gradients exist in a 40 μm thick region near the edge. The rest of the sample retains the equilibrium gas concentration, as seen by the flat regions in the center of the profiles. This indicates that the desorption step does not significantly alter the local gas concentration across the sample. Consequently, a high cell nucleation density of the order of 10^{14} cells/cm^3 is observed in the 500 μm film, producing a porous, open-cell nanocellular structure. All features are identical to the corresponding structure observed in PEI bulk specimens under these conditions.

The gas concentration profile of the 250 μm film is comparable to that of the 500 μm film. Despite the similarity in the profiles of the two films, the microstructures differ significantly. The current model cannot distinguish the precise conditions of local gas concentration under which these two distinct microstructures develop. The AGCs required to create both structures are in a very close range between 100–110 mg/g [32], and a detailed analysis of the cell nucleation and growth needs to be conducted to understand the evolution of such nano-morphologies. Nevertheless, the presence of ultra-fine cells of the order 70 nm in the 250 μm film enables a 20% higher porosity than the 500 μm film.

In the 120 μm film, the AGC before foaming drops to 93 mg/g, which is 15% gas loss from equilibrium saturation. Figure 2 shows that concentration gradients exist in a 30 μm thick region near the edge. Thus, only 50% of the sample retains the equilibrium gas concentration. Compared to the 500 and 250 μm film, this is a larger gradient resulting in two orders of magnitude lower cell nucleation density and 50% lower porosity.

In the 70 μm film, the gas concentration before foaming is reduced to 83.5 mg/g, and the gradient in local concentration across the thickness, as seen in Fig. 2, is considerably higher. Only a small part (10 μm length, 14%) of the sample retains the local gas concentration at equilibrium, and gradients exist in 86% of the sample. Interestingly, there is a stark contrast between the concentration profiles and the microstructure observed. Despite the continuous gradient in the profile, a uniform structure is observed across the thickness, as can be seen in Fig. 4. It is known that the structure observed in the 70 μm film is a low gas concentration structure, usually observed near the solid skin in bulk specimens. It is possible that right before foaming, the global concentration in the sample dropped below the minimum required concentration to produce a structure in which the primary cell size is in the nanometer regime, resulting in a uniform low gas concentration structure. Furthermore, the emergence of a secondary nanocellular structure within the cell walls strongly suggests a subsequent nucleation event. This event occurs once the primary cells have attained a critical size. The genesis of this secondary nucleation is linked to the considerable strain energy build-up in the polymer as the microcells take shape, eventually triggering a 'crazing' phenomenon in the cell walls. This strain-induced nucleation process results in the formation of nanocells within the cell walls of the primary microcellular structure, as illustrated in (Fig. 3), and is also observed in other polymers like polycarbonate [36, 37]. Despite this unique architecture, this film does not exhibit any porosity, possibly because the nanopores in the cell walls are not interconnected through the foam to create a permeable network.

For the 25 μm film, one-minute desorption resulted in a significant gas loss, as can be seen from Fig. 2. Due to this, the film could not be foamed. The AGC in the film after 1-minute desorption was around 57.5 mg/g. Previously, Miller et al. could produce a cellular structure for the same AGC in a 1.5 mm thick PEI specimen [20]. If we look at the local gas concentration profile in Fig. 2 we see a high gradient across the profile, and the peak concentration is much lower than the equilibrium concentration. This shows that the kinetics of the desorption process in the 25 μm film prevents the development of any cellular structure. The gas loss in 1 min depletes the gas concentration in the entire film to below the minimum concentration needed for cell

nucleation [7]. Therefore, no cellular structure develops in the film.

Future directions

As nanocellular polymer thin films find increasing applications, characterizing their properties to understand the effect of cell size and other microstructure features becomes even more important. Some properties of immediate interest are the dielectric constant, fracture toughness, tear resistance, permeability, and thermal insulation. To produce a foamed film with a given cell size, morphology, skin thickness, and relative density would require computational models that can take multiple process variables and predict the final structure. This, combined with an understanding of the properties of different structures, would enable us to create highly engineered materials. In terms of fabrication, developing pressure vessels that can foam films at the instant of depressurization would facilitate the foaming of even thinner films. Low-temperature saturation would also be a potential solution as it would increase the total gas concentration in the structure, thus compensating for the gas loss during desorption. We performed several low-temperature experiments on the 25 μm film and were able to foam it successfully. Thus, the world of solid-state foamed thin films is full of unexplored possibilities with great potential in scientific knowledge and technological development.

Concluding remarks

Thus, we explored the evolution of nanocellular structure in PEI thin films with thicknesses between 25 μm and 500 μm. Solid-state foaming resulted in distinct cellular morphologies, transitioning from an open-cell nanocellular structure in the thick film to a closed-cell hierarchical structure in the thinnest film. The primary cell size varied over two orders of magnitude, from 70 nm to 2 μm. Gas loss and relative density increased with decreasing thickness. The variation in cell size and cell nucleation density altered the pore surface areas of these materials, creating both porous and non-porous foams. Modeling the gas concentration profiles across the thickness of a desorbing polymer film revealed local gas concentration to be the primary driver of nanostructure development. This study underscores the exceptional degree of structural tunability offered by the solid-state process, allowing the creation of polymers with tailored gas concentration profiles. Importantly, these unique structures hold the potential for intriguing variations in thermal conductivity, dielectric constant, permeability, and fracture toughness, which warrant further investigation. Future research examining even thinner films and exploring their associated properties will pave the way for developing lightweight materials that are easily manufacturable and possess a broader range of properties than their solid counterparts.

Acknowledgements

Author contributions

ZSP, VK, and KN conceptualized the research, ZSP performed the experiments and developed the model, AN performed porosimetry experiments and AN, CJ, and SS analyzed the data, ZSP and VK wrote the first draft of the manuscript, and all authors finalized the manuscript.

Data and code availability

All data are available in the manuscript, and additional information can be provided upon reasonable request.

Declarations

Conflict of interest   The authors declare no conflict of interest.

Ethical approval   Not applicable

Supplementary information   Not applicable

References

[1] Dingcai W, Fei X, Sun B, Ruowen F, He H, Matyjaszewski K (2012) Design and preparation of porous polymers. Chem Rev 112(7):3959–4015

[2] Jiang J-X, Laybourn A, Clowes R, Khimyak YZ, Bacsa J, Higgins SJ, Adams DJ, Cooper AI (2010) High surface area contorted conjugated microporous polymers based on spiro-bipropylenedioxythiophene. Macromolecules 43(18):7577–7582

[3] Ma X, Lai HWH, Wang Y, Alhazmi A, Xia Y, Pinnau I (2020) Facile synthesis and study of microporous catalytic arene-norbornene annulation-troger's base ladder polymers for membrane air separation. ACS Macro Lett 9(5):680–685

[4] Martini-Vvedensky Jane E, Suh Nam P, Waldman, Francis A (1984) Microcellular closed cell foams and their method of manufacture, September 25. US Patent 4,473,665

[5] Kumar V, Weller JE (1993) A process to produce microcellular pvc. Int Polym Proc 8(1):73–80

[6] Collias DI, Baird DG, Borggreve RJM (1994) Impact toughening of polycarbonate by microcellular foaming. Polymer 35(18):3978–3983

[7] Kumar V, Weller JE (1994) A model for the unfoamed skin on microcellular foams. Polym Eng Sci 34(3):169–173

[8] Murray RE, Weller JE, Kumar V (2000) Solid-state microcellular acrylonitrile-butadiene-styrene foams. Cell Polym 19(6):413–425

[9] Victoria Nawaby A, Paul Handa Y, Liao X, Yoshitaka Y, Tomohiro M (2007) Polymer-co2 systems exhibiting retrograde behavior and formation of nanofoams. Polym Int 56(1):67–73

[10] Shimbo M, Higashitani I, Miyano Y (2007) Mechanism of strength improvement of foamed plastics having fine cell. J Cell Plast 43(2):157–167

[11] Paul Handa Y, Wong B, Zhang Z, Kumar V, Eddy S, Khemani K (1999) Some thermodynamic and kinetic properties of the system petg-co2, and morphological characteristics of the co2-blown petg foams. Polym Eng Sci 39(1):55–61

[12] KurnaW V, Juntunena P (2000) Impact strength of high relative density solid state carbon dioxide blown crystallizable poly (ethy1ene terephthalate) microcellular foams. Cell Polym 19(1):25

[13] Kumar V, Gebizlioglu OS et al (1991) Carbon dioxide induced crystallization in pet foams. SPE Tech Pap 37:1297–1299

[14] Wang X, Kumar V, Li W (2007) Low density sub-critical co2-blown solid-state pla foams. Cell Polym 26(1):11–35

[15] Park CB, Suh NP, Baldwin DF (1999) Method for providing continuous processing of microcellular and supermicrocellular foamed materials, February 2. US Patent 5,866,053

[16] Paul Handa Y, Zhang Z (2000) A new technique for measuring retrograde vitrification in polymer-gas systems and for making ultramicrocellular foams from the retrograde phase. J Polym Sci, Part B: Polym Phys 38(5):716–725

[17] Hedrick JL, Carter KR, Cha HJ, Hawker CJ, DiPietro RA, Labadie JW, Miller RD, Russell TP, Sanchez MI, Volksen W et al (1996) High-temperature polyimide nanofoams for microelectronic applications. React Funct Polym 30(1–3):43–53

[18] Bernd Krause G-H, Koops NFA, van der Vegt M, Wessling MW, van Turnhout J (2002) Ultralow-k dielectrics made by supercritical foaming of thin polymer films. Adv Mater 14(15):1041–1046

[19] Bemed Krause HJP, Sijbesma PM, Van der Vegt NFA, Wessling M (2001) Bicontinuous nanoporous polymers by carbon dioxide foaming. Macromolecules 34(25):8792–8801

[20] Miller D, Chatchaisucha P, Kumar V (2009) Microcellular and nanocellular solid-state polyetherimide (pei) foams using sub-critical carbon dioxide i. processing and structure. Polymer, 50(23):5576–5584

[21] Miller D, Kumar V (2011) Microcellular and nanocellular solid-state polyetherimide (pei) foams using sub-critical carbon dioxide ii. tensile and impact properties. Polymer, 52(13):2910–2919

[22] Guo H. (2015) Solid-state polymer nanofoams. Ph.D thesis

[23] Guo H, Kumar V (2015) Some thermodynamic and kinetic low-temperature properties of the pc-co2 system and morphological characteristics of solid-state pc nanofoams produced with liquid co2. Polymer 56:46–56

[24] Wang G, Najafi F, Ho K, Hamidinejad M, Cui T, Walker GC, Singh CV, Filleter T (2022) Mechanical size effect of freestanding nanoconfined polymer films. Macromolecules 55(4):1248–1259

[25] Xia W, Keten S (2015) Size-dependent mechanical behavior of free-standing glassy polymer thin films. J Mater Res 30(1):36–45

[26] Feng T, He J, Rai A, Hun D, Liu J, Shrestha SS (2020) Size effects in the thermal conductivity of amorphous polymers. Phys Rev Appl 14(4):044023

[27] Pfeiffenberger N, Milandou F, Niemeyer M, Sugawara T, Sanner M, Mahood J (2018) High temperature dielectric polyetherimide film development. IEEE Trans Dielectr Electr Insul 25(1):120–126

[28] Tan D, Zhang L, Chen Q, Irwin P (2014) High-temperature capacitor polymer films. J Electron Mater 43:4569–4575

[29] ASTM Committee D-20 on Plastics (2008) Standard test methods for density and specific gravity (relative density) of plastics by displacement. ASTM international

[30] Kumar V, Suh NP (1990) A process for making microcellular thermoplastic parts. Polym Eng Sci 30(20):1323–1329

[31] Nicolae A (2018) Advanced methods to produce and characterize transport properties of novel nanoporous polymers. Ph.D thesis

[32] Zhou C, Vaccaro N, Sundarram SS, Li W (2012) Fabrication and characterization of polyetherimide nanofoams using supercritical co2. J Cell Plast 48(3):239–255

[33] Brunauer S, Emmett PH, Teller E (1938) Adsorption of gases in multimolecular layers. J Am Chem Soc 60(2):309–319

[34] Bardestani R, Patience GS, Kaliaguine S (2019) Experimental methods in chemical engineering: specific surface area and pore size distribution measurements-bet, bjh, and dft. Can J Chem Eng 97(11):2781–2791

[35] Nagendra B, Cozzolino A, Daniel C, Rizzo P, Guerra G (2022) High surface area nanoporous-crystalline polymer films. Macromolecules 55(7):2983–2990

[36] Gong P, Taniguchi T, Ohshima M (2014) Nanoporous structure of the cell walls of polycarbonate foams. J Mater Sci 49:2605–2617

[37] Van Loock F, Bernardo V, Pérez MAR, Fleck NA (2019) The mechanics of solid-state nanofoaming. Proc R Soc A 475(2230):20190339